ASTFE
American Society
of Thermal and Fluids Engineers

4th Thermal and Fluids Engineering Conference (TFEC)
April 14–17, 2019
Las Vegas, NV, USA

TFEC-2019-27620

A PARAMETRIC STUDY ON DRAG REDUCTION USING ENGINEERED MICROTEXTURES IN VISCOUS LAMINAR FLOW

Pooyan Tirandazi, John Healy, Carlos Hidrovo*

Northeastern University, Boston, MA 02115, USA

ABSTRACT

The topic of friction reduction has been studied through the decades for numerous engineering applications that involve internal and external flows. Inspired by the natural surface structure of different plants and animals, engineered microtexturing of surfaces is one of the effective ways of reducing the drag. By introducing different texture geometries, the flow behavior close to the solid boundary can be altered and thus manipulated towards achieving a reduced net drag force on the surface. Despite considerable research on the subject, most works have concentrated on optimization of the surface texturing for maximizing the friction reduction and minimizing the pumping power requirements, and less attention has been paid to characterization of the flow and boundary layer in the vicinity of the wall, especially in laminar regime. In this work we investigate the role that microtexturing has on friction reduction under low to moderate Reynolds numbers (*Re*). We perform a parametric study on the shape and dimensions of the surface textures and investigate the boundary layer and streamline behavior as well as the local shear stress and pressure distribution along the solid-fluid interface under different flow conditions. The outcomes of this work will provide a guideline for optimal design of artificial textures with major implications for many engineering applications such as microfluidic systems used in thermal management and biochemical diagnostics.

KEY WORDS: drag reduction, textured surface, laminar flow, boundary layer, viscous flow

1. INTRODUCTION

Reducing the drag that is exerted by a fluid flow has many engineering implications for energy saving. Different techniques have been adopted over the years to achieve a reduced drag in applications that concern external flow around objects (*e.g.* transportation systems such as cars, ships, and airplanes) and internal flows (*e.g.* transfer of fluids through channels or pipes) [1]. Addition of certain polymers for example has been repeatedly shown to reduce the drag in turbulent pipe flow up to 80% [2], [3]. Another common technique for drag reduction includes modification of the surface by creating microtextures at the solid-fluid interface. Such textures, usually inspired by the natural surface structure of different animals (such as sharks skins) and plants (such as lotus leaf), have been shown to effectively reduce the drag exerted by the flow [4], [5]. The presence of textures on a surface can induce unique flow behaviours by altering the boundary layer adjacent to the wall, resulting in a reduced net drag. Recent advances in microfabrication techniques have made it possible to create engineered microtextures with controlled microgeometries on the surfaces to systematically investigate the net drag force exerted by the flow. A variety of geometries such as ribs, trenches, and pillars have been studied for this purpose [2], [6]. Most of the research in this area however, has focused on reducing skin friction in the turbulent regime. For example, several works have investigated the use of longitudinal riblets in the turbulent regime and have shown up to 10% reduction in drag [7], [8]. A more recent study on the effect of streamwise riblets in the laminar regime has also shown that riblets exhibiting a width to height aspect ratio close to unity represent the highest reduction in the drag force up to 20% [9].

*Corresponding Author: hidrovo@neu.edu

With the emergence of microfluidic systems, new challenges have arisen to engineer the flow in small domains such as microchannels [10]. As a consequence, drag reduction in the laminar and sub-laminar regimes has become an important topic area, with the development of highly efficient microfluidic systems for biomedical analysis and thermal treatment applications holding high economic value [11]. Several works investigating pressure-driven flow inside microchannels with textured walls considered the hydrophobicity of different surface geometries. These studies have mostly focused on understanding the wetting transition and attempted to maintain the Cassie state by sustaining the air-water interface in the microstructures [12]–[17]. In this state, due to the presence of the so-called shear-free zones at the gas-liquid interface, movement of the liquid film is facilitated. Lubricant-impregnated surfaces have also been reported as an effective way to achieve up to 16% drag reduction by introducing lubricating liquids (instead of air) inside the trenches [18].

In this work we examine the drag properties of an external liquid flow over a flat plate with transverse trenches on the surface. In comparison to streamwise riblets, spanwise trenches are scarcely covered in the literature, especially in the laminar regime. Moreover, we focus here on the fully wetted Wenzel state in contrast to the Cassie state. We use numerical modelling to simulate single-phase liquid flow for moderate Reynolds numbers in the laminar regime ($2\times10^3 < Re_L < 2\times10^4$). We first provide the validation of the numerical model for the case of a flat plate and compare it to the Blasius solution. Next, we consider different arrays of rectangular trenches and investigate the flow and streamlines in the presence of such textures. We discuss the effect that trenches have in terms of the shear and pressure components of the drag and compare different trench aspect ratios. It is demonstrated that the trapped vortical flow patterns that are formed within the trenches in the Wenzel state are able to provide drag reduction at certain spacings by allowing the mainstream flow to slide on top of them.

2. METHOD

Using numerical techniques, the physics of geometrically induced drag reduction can be studied more comprehensively than experimental methods. For the presented study, the steady-state Navier-Stokes equations were solved numerically for fluid velocity and pressure distributions in a 2D fluid domain. By employing the finite volume method and the SIMPLE (Semi implicit Method for Pressure Linked Equations) algorithm, the velocity (u, v) and pressure (p) gradients can be extracted in detail at small length scales [1]. SIMPLE solves by coupling the velocity field with the pressure field, starting each iteration with an initial guess for the pressure and velocity gradients, computing the mass flux through a finite volume, then applying correction factors to the initial guess. Convergence is checked with a supplied criterion at each iteration, if the solution convergence at a given iteration is greater than the criterion, the next iteration is started. If the solution has converged below the criterion, the solver is terminated. Residual convergence criterion was set to 10^{-6} for results shown. The numerical solver requires inputs in the form of a discretised geometry, boundary conditions, and process fluid properties. In the results presented below, the process fluid is liquid water at STP (ρ= 998.2 kg/m^3, μ= 0.001003 kg/m.s).

The computational domain, as shown in fig. 1a, was $L_x \times L_y$ = 51mm × 38mm. L_x includes a 3mm slip boundary on the leading edge of the 48mm streamwise no-slip wall. It has been shown that due to the expected singularity at the leading edge of a plate in external flow, extending the computational domain by means of a slip surface upstream of the no-slip wall allows for accurate pressure and velocity response in the domain. This produces a more accurate C_d when compared to boundary conditions where the leading edge effects are not considered. Multiple inlet symmetry lengths were studied, and the optimum length was chosen such that the velocity profile of the flat plate case is within 1% of the accepted Blasius solution.

To complete the computational setup, a uniform velocity inlet was imposed on the left boundary, and a uniform pressure outlet was imposed on the right and top boundaries. L_y was chosen such that negligible fluid shear was observed at the upper boundary of the domain. Internal studies have also shown accuracy in numeric flat plate simulations with domain heights 10x the expected boundary layer thickness. Through this study, focus is placed on anti-streamwise trenches added to the plate with sharp, square edges in a range of geometrical aspect ratios. The geometry is defined by three dimensional parameters, A, B, and C, as seen in Fig. 1b. Through the cases studied, L_x was kept constant while the depth (C) and length (B) of the valley features were altered. Changes to B and C were made ensuring a whole number of valley feature iterations in the stream-wise direction

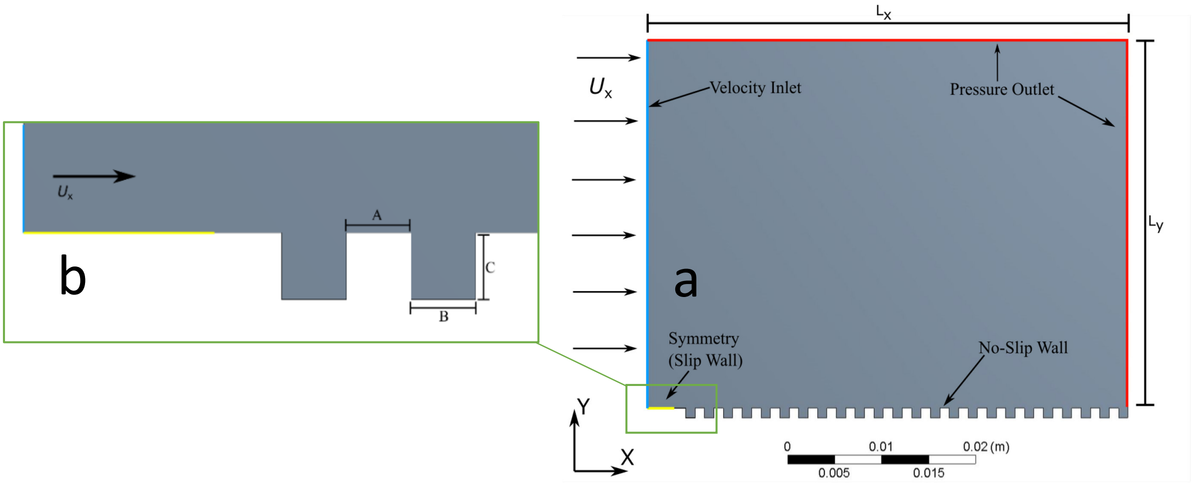

Fig. 1 (a) Diagram of the computational fluid domain and boundary conditions; (b) Detail view of the wall texture parameters A, B, and C.

2.1 Grid Resolution Study

The mesh used for the cases presented in this paper was optimized for the simulation geometry and mesh independence was verified. For all simulations, average mesh size in the domain was 80µm. Mesh size was refined to 20µm closer to the walls to accurately capture boundary layer activity. This refinement was also made on the corners and interior of the valley features as shown in Fig. 2b to capture fluid behaviour inside the valley. Total element counts for simulations ranged from $N=5\times10^5$ to $N=1.5\times10^6$ due to geometrical and flow regime changes.

With focus placed on the case of a flat plate in uniform laminar external flow, mesh independence can be checked using the drag coefficient derived from simulation results. The drag coefficient from l_0 to l_w on the plate per unit length in the z direction is given by the following equation

$$C_D=\frac{F_D}{\frac{1}{2}\rho U^2 l_w}=\frac{1}{\frac{1}{2}\rho U^2 l_w}\int_{l_0}^{l_w}\tau_w\, dl \tag{1}$$

Where F_D is the drag force reacted by the plate, U is the free stream fluid velocity, and l_w is the total length of the wall. In Fig. 2a below, C_D of flat plate flow is given at U=0.1 m/s (Re_L = 4770). The dotted line represents the Blasius solution for the laminar drag coefficient $C_D=1.328/\sqrt{Re_L}$. Element count was increased, and mesh was refined until C_D varied less than 1% from the Blasius solution.

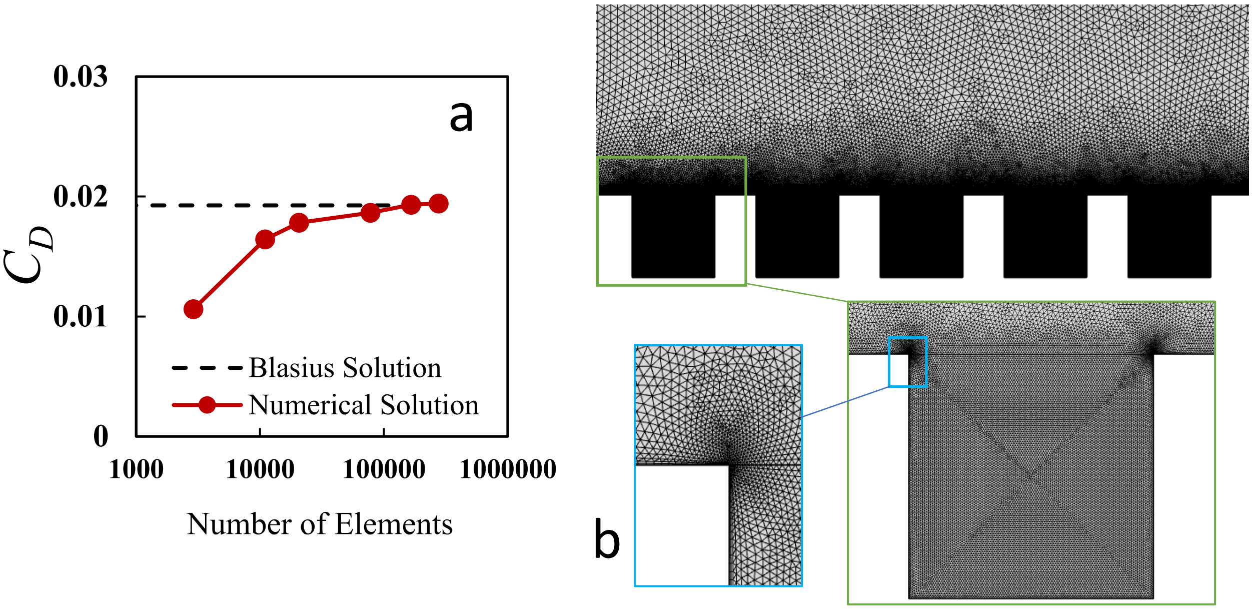

Fig. 2 (a) Plot of C_D versus the number of elements in the computational domain, mesh refinement method was kept consistent with higher mesh densities closer to the plate surface to capture boundary layer effects; (b) Unstructured mesh refinement inside valley features and around sharp corners.

2.2 Flat Plate Validation Study

To validate the simulation boundary conditions, a characteristic benchmark of laminar flow over a flat plate was used for comparison. For this validation study, the domain and boundary conditions presented in the section above remained the same, save for the valley features. A flat 48 mm no-slip wall was placed in a uniform flow of liquid water (ρ= 998.2 kg/m^3, μ= 0.001003 kg/m-s) at a velocity of U_{in}=0.1m/s. The local *Reynolds* number at the end of the flat plate given by $Re_L=\rho U_{max} L/\mu$, was laminar at 4770.

This simulation solution was then compared to the Blasius solution describing the laminar velocity boundary layer over a flat plate. The Blasius solution states that given the nondimensional similarity variable $\eta = y\sqrt{U/\nu x}$, the nondimensional x-component of the velocity u/U is a function of η complying with the momentum equations for a boundary layer. Where u is the x-component of a fluid velocity at (x,y) in Cartesian space, U is the free stream velocity, and ν is the fluid kinematic viscosity. Using the numerically calculated solution of a laminar flat plate velocity profile with respect to η, the benchmark simulation results are validated with theory in Fig. 3a below. As shown, the simulation results and theoretical solution match within 1%, suggesting accurate boundary conditions and domain dimension.

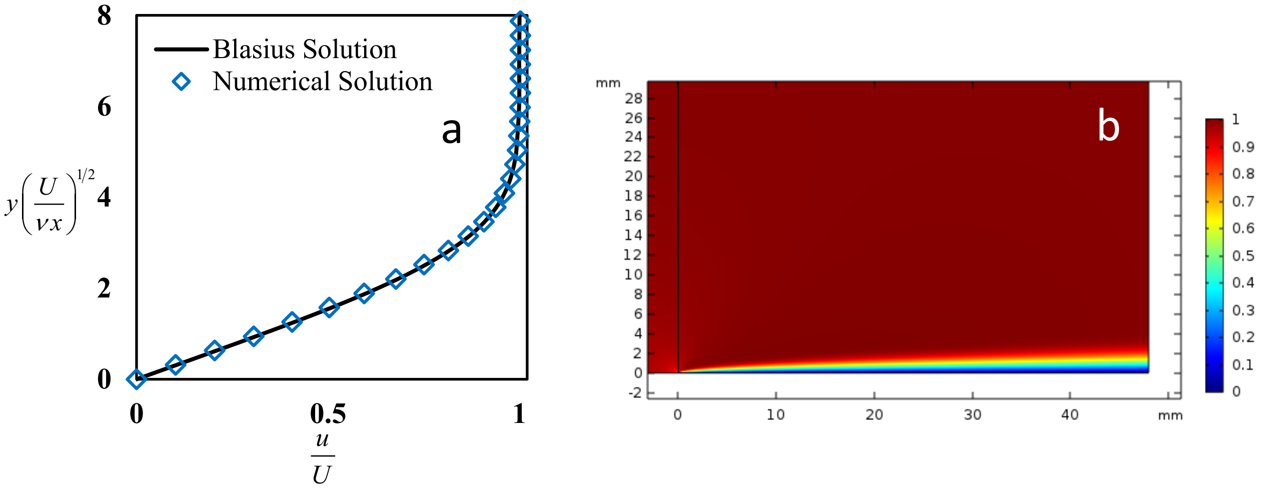

Fig. 3 (a) Results of simulation results with the classical flat plate boundary layer theory at Re_L=4770, the theory and results show strong agreement; (b) Contour of relative fluid velocity (u/U) of the characteristic laminar boundary layer over a flat plate.

3. RESULTS AND DISCUSSIONS

After validating the results of a flat plate, we now consider the flow over a plate that contains transverse trenches. The geometrical features studied in this work consists of arrays of rectangular 2D trenches specified by a width (B) and height (C). Introduction of these trenches alter the flow adjacent to the wall that could increase or decrease the drag over the surface. Although the drag force on a flat plate is solely due to friction drag which is an effect of the wall shear stress, for trenches normal to the flow direction, the contribution of pressure forces cannot be discounted. Pressure force contribution should be taken into account in addition to the shear forces since the velocity and pressure fields can be substantially affected by the presence of trenches in the flow. Fig. 4 shows a comparison of computational results for the distribution of pressure and shear stress along the plate at Re_L=4770. In the plot, the shear and pressure distributions for the textured geometry are calculated along the line that passes over the trenches where the mainstream is moving. Both the local pressure and shear stress are nondimensionalized by the dynamic pressure of the free stream ($\frac{1}{2}\rho U^2$). As the flow approaches the trench from left, a low-pressure zone is built near the leading (left) corners of the trench while the trailing (right) corners act oppositely by creating a stagnation high-pressure zone. Therefore, the pressure distribution reveals an evidence of drag increase instead of drag reduction in this type of geometry. By looking at the shear stress distribution we can see that the at the corners there always exist an upward spike representing an increase in the local shear stress at both leading and trailing corners of a trench. However, the regions that correspond to the flow passing over a trench represent a near-zero shear which can be considered as shear-free region that can contribute to flow slip and thus, reduction in the total drag over the surface.

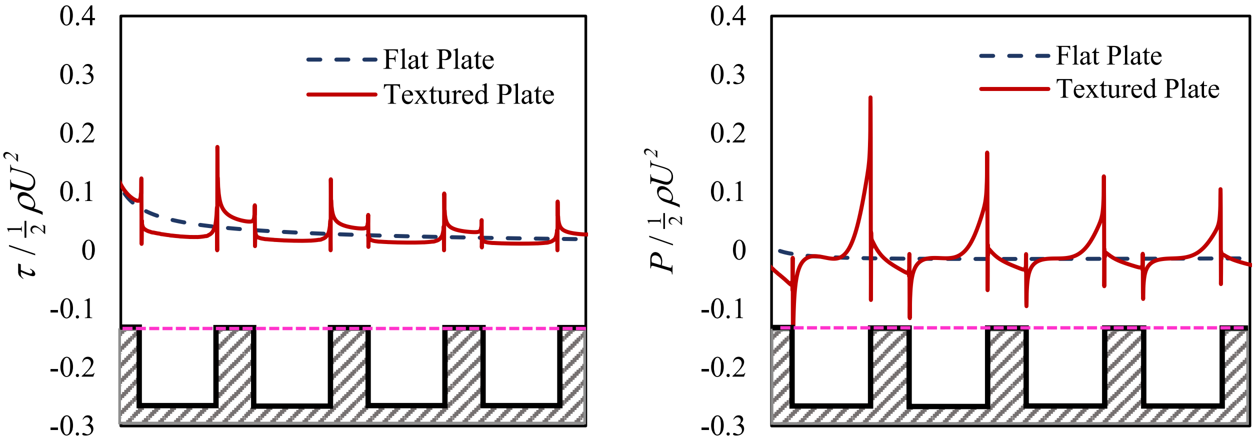

Fig. 4 Distribution of the nondimensional shear stress (left) and pressure (right) for a flat plate and a plate with rectangular trenches at Re_L=4770. The local shear and pressure are evaluated along the imaginary line over the valleys (the magenta line). Introducing the trenches in in the plate induces multiple spikes at the location of the corners. However, the regions where flow is passing on top of a trench features near-zero shear.

Different combinations of trench depths and widths are simulated and compared to assess the effect of the geometry on the flow and drag. We first consider each component of the drag, namely the skin friction due to shear stress and the pressure drag. Fig. 5 shows the behavior of shear and pressure components of the drag in terms of drag coefficients ($C_{D,\text{ shear}}$ and $C_{D,\text{ pressure}}$) which are defined as:

$$C_{D,\text{ shear}} = \frac{F_{D,\text{ shear}}}{\frac{1}{2}\rho U^2 L_w} \tag{2}$$

$$C_{D,\text{ pressure}} = \frac{F_{D,\text{pressure}}}{\frac{1}{2}\rho U^2 L_w} \tag{3}$$

where $F_{D,\text{ shear}}$ and $F_{D,\text{ pressure}}$ are the contribution of shear and pressure forces acting on the wall that are evaluated from the numerical results by integration of the local pressure and shear over the entire wetted wall. L_w represents the total length of the wall which contains the extra length due to addition of trenches. For all the trench depths simulated here (0.5mm, 1mm, and 2mm) pressure and shear drag have opposing behavior as trench width (B) is increased. Pressure drag, shown as $C_{D,\text{ pressure}}$, demonstrates an initial increase reaching a maxima and decaying, while $C_{D,\text{ shear}}$ values initially decrease and reach a minimum as the trenches become wider. The initial decreasing trend in $C_{D,\text{ shear}}$ can be attributed to two phenomena. As the trenches get wider, the ratio of trench to land region increase in the same domain length (48mm). As a result, a larger portion of the flow feel the partial slip condition provided by the trenches. Moreover, widening the trenches reduces the number of corners density with respect to the total plate length. Each corner acts like the leading edge of a plane which represents a high initial shear as can be seen in Fig. 4. Therefore, as the trenches get wider while maintaining the total plate length, the population of the corners decreases leading to the reduction of $C_{D,\text{ shear}}$. By looking at the flow streamlines shown in Fig. 6, it can be seen that smaller trenches can sustain the recirculating flow within them leading to partial slip of the flow that moves above them. However, vortical patterns which envelop the entire trench cannot hold for trenches beyond a certain aspect ratio. This leads to vortex instability and the development of a different flow behavior resulting in the main flow contacting the bottom of each trench causing $C_{D,\text{ shear}}$ to increase again. To understand the contribution of pressure, we should also consider the vertical walls inside the trenches. As the trenches become wider, the main flow streamlines bend more while passing over a trench, causing the flow to hit a bigger portion of the trailing wall. This will increase the total pressure drag that is felt against the flow. As the number of trenches decrease, the number of these trailing walls would also decrease which results in an overall reduction in $C_{D,\text{ pressure}}$. It is worth noting that the trench aspect ratio is an important parameter that affects both $C_{D,\text{ pressure}}$ and $C_{D,\text{ shear}}$ behavior. The results of $C_{D,\text{ pressure}}$ and $C_{D,\text{ shear}}$ for different trenches can be plotted against the trench width to depth aspect ratio (B/C) as shown in Fig. 7. It can be seen that the maximum for $C_{D,\text{ pressure}}$ and minimum for $C_{D,\text{ shear}}$ for different trench widths collapse in the x direction and occur when the aspect ratio of trenches is approximately 10 for this particular Re_L (~4770).

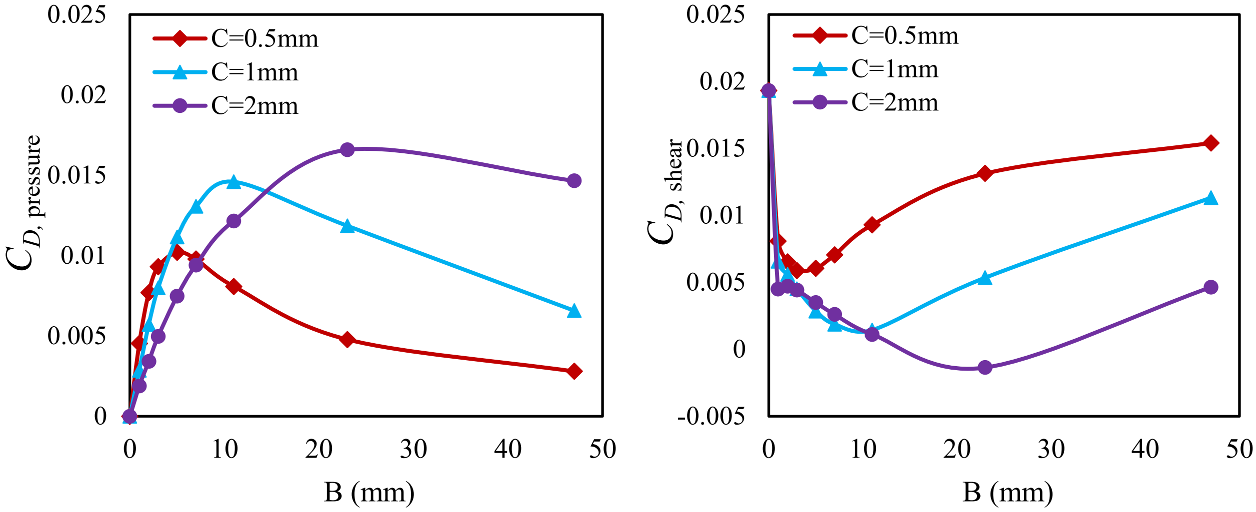

Fig. 5 Comparison of the pressure drag coefficient ($C_{D,\text{ pressure}}$) (left) and the frictional drag coefficient ($C_{D,\text{ shear}}$) (right) for different trench depths and widths. Note the B=0 represents a flat plate.

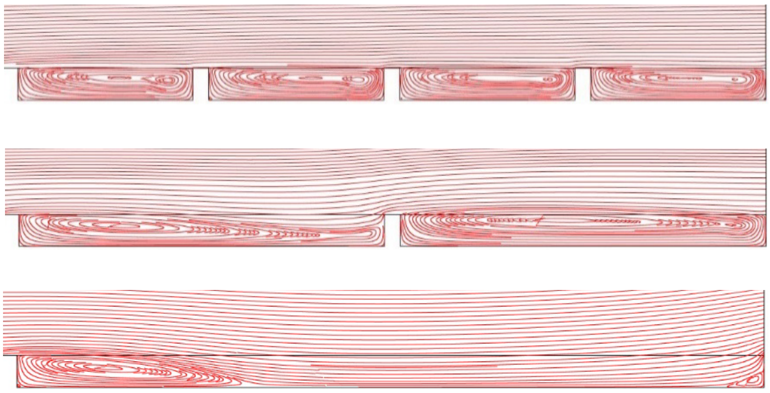

Fig. 6 Flow streamline behavior for different trench spacing at Re_L=4770. The above trenches contain the same depth (C=2mm). The width to depth aspect ratio of the trenches play an important role in sustaining the vortices in the valleys. High aspect ratios lead to break down of the circulating structure beneath the main flow causing it to reach the bottom of the trench and experience addition shear of the bottom surface.

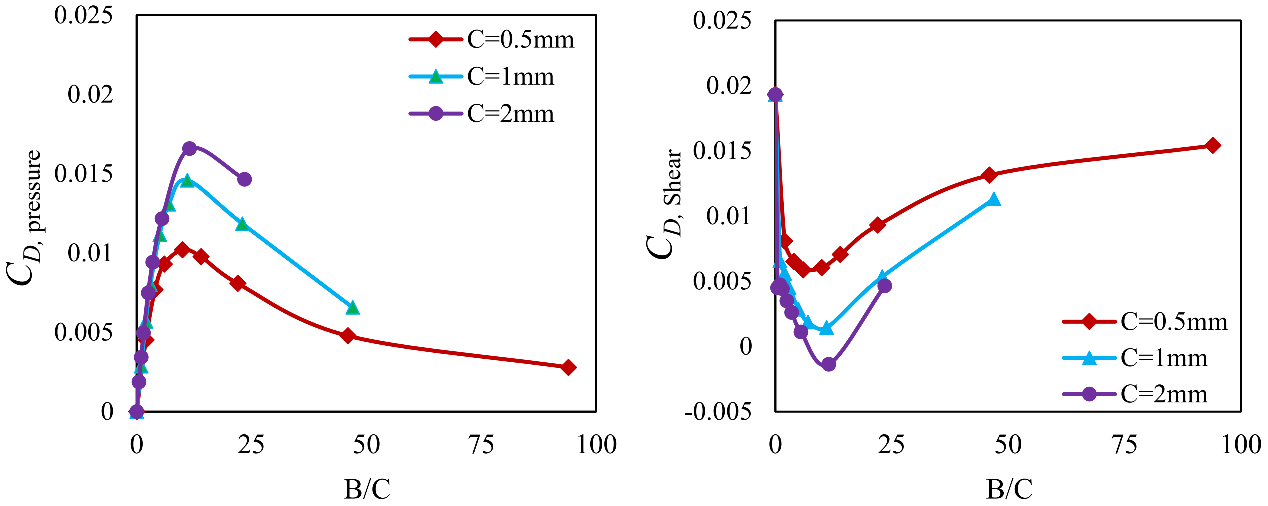

Fig. 7 Comparison of the pressure drag coefficient ($C_{D,\text{ pressure}}$) (left) and the frictional drag coefficient ($C_{D,\text{ shear}}$) (right) based on trench aspect ratio.

To characterize the effectiveness of the trenches, both shear and pressure contributions should be considered. Therefore, we evaluate the changes in total drag coefficient (C_D) which is the sum of $C_{D,\text{ shear}}$ and $C_{D,\text{ pressure}}$, and total drag force in comparison to the flat plate. Fig. 8 shows the change in C_D and drag force for different trench widths and depths. The negative values in the plots represent a reduction of drag coefficient as compared to the flat plate. For all different combinations of trenches, the reduction in the shear part overcomes the increase in the pressure coefficient. The results show a significant reduction in the total friction coefficient down to about 67%. However, these reductions can be misleading as introducing trenches increases the total length of the plate. Therefore, the total drag force that is calculated by integrating both the pressure and shear components over the walls of the plate represents a more realistic metric for evaluating the true role of microtexturing on drag. The results of the total drag force are also shown in Fig. 8. It is evident that the increase in the length of the plate due to addition of trenches significantly contributes to the total drag behavior. It can be seen that for a deeper trench, as the trench width increases the total drag force initially decreases and reaches a minimum of about 10%. However, further increase in the trench width can even cause an increase of the total drag in comparison to the flat plate despite having a negative C_D.

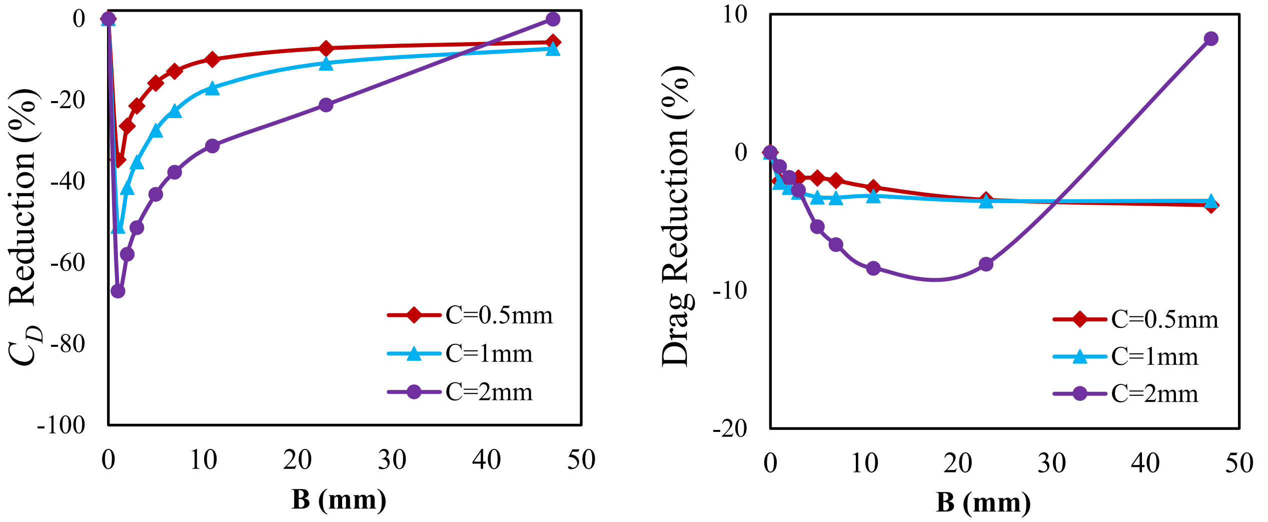

Fig. 8 Percentage reduction in the total drag coefficient (left) and total drag force (right). Although for all different trench geometries the drag coefficient shows a negative value (reduction). When the total length of the plate with trenches are calculated in the drag force, the reduction goes to a minimum of 10%. Moreover, wider valleys would allow the flow

to enter the trench and feel the addition shear force from the bottom of the trenches which adds up to the corner effects of trenches and results in an increase in the value of total drag force in comparison to a simple flat plate.

Lastly, we examine the change of the total drag force as a function of Re_L. Different Re_L are obtained by increasing the inlet velocity in the simulations keeping the same length for the computational domain. In Fig. 9 the total drag force reduction for four different trench widths with the same depth (2mm) are compared over different Re_L. As mentioned before, the total drag force takes into account the entire wetted length of the plate including the added length due to the trench walls. For the narrower trenches, as long as the vortical structure inside the trench is maintained, smaller number of trenches with wider trenches are preferred. As the Re_L increases, the flow can skip over the trenches more efficiently instead of protruding into the trenches. Therefore, a slight reduction can be observed at higher Re_L. However, for the widest trench simulated in this study (B=47mm), the flow reached the bottom of the trench for all the Re_L. Hence, the total drag force is increased due to the lack of slip zones under the flow. Moreover, the presence of the trench in the flow causes high pressure forces on the upstream facing vertical walls which would increase the total drag further.

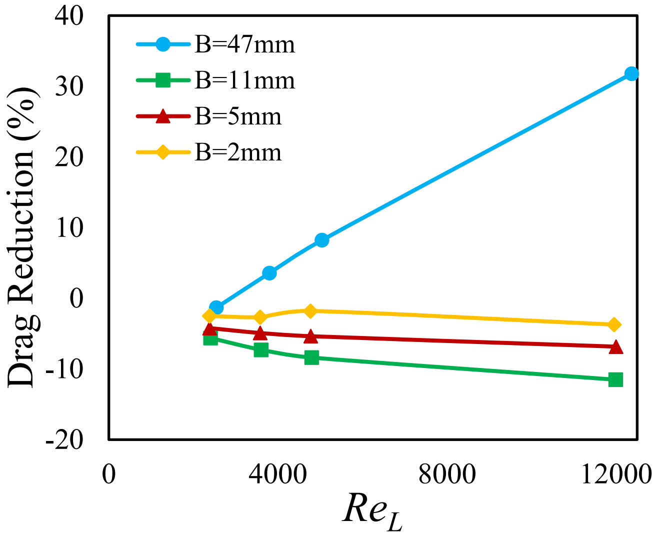

Fig. 9. Total drag reduction as a function of Re_L. Different Re_L are achieved by increasing the inlet velocity in the simulations while the total length of the computational domain remains constant. For calculating the drag force however, the entire length of the plate is considered which includes the addition of trench walls.

4. CONCLUSIONS

Passive reduction of fluid drag can be achieved by introducing microtextures on a surface which could save energy and benefit many engineering disciplines. In this work we have numerically studied drag reduction in viscous laminar flows over a surface. We have used spanwise rectangular trenches and investigated different combination of trench sizes in the fully wetted Wenzel state. The flow behavior in the presence of trenches are studied and the main components of drag force, namely the pressure drag and the shear drag are evaluated for different aspect ratios of the trench dimensions. It has been shown that at certain trench sizes a single vortical flow pattern can be formed inside the trenches. These vortices are responsible for partial slip of the flow over the trenches which can provide less drag in comparison to a flat plate case. If these trenches however, become wider than a certain ratio, the streamlines will bend and protrude into the trench region and break the contained vortical flow. In this situation, the main flow interaction with the no-slip wall at the bottom of the trenches would contribute to an increase in shear over the contained vortex case. Moreover, the adverse pressure effects from the vertical walls of the trench can further add to the drag force which together with the shear forces induced by bottom surface of the trenches result in a drag increase in comparison to a flat plate case.

ACKNOWLEDGMENT

This work is supported by National Science Foundation (NSF), award number 1705958.

NOMENCLATURE

L_x	Computational Domain Length	(m)	ρ	Density	(kg/m^3)
L_y	Computational Domain Height	(m)	U	Inlet Velocity	(m/s)
L_w	Wall Length	(m)	$C_{D,\ \mathrm{pressure}}$	Pressure Drag Coefficient	(-)
Re_L	fourth variable	(-)	$C_{D,\ \mathrm{shear}}$	Shear Drag Coefficient	(-)
A	Land Region Width	(m)	C_D	Total Drag Coefficient	(-)
B	Trench Region Width	(m)	P	Pressure	(Pa)
C	Trench Region Depth	(m)	τ	Shear Stress	(Pa)

REFERENCES

[1] G. Yunqing, L. Tao, M. Jiegang, S. Zhengzan, and Z. Peijian, “Analysis of Drag Reduction Methods and Mechanisms of Turbulent,” *Appl. Bionics Biomech.*, vol. 2017, 2017.

[2] Q. Bai, J. Bai, X. Meng, C. Ji, and Y. Liang, “Drag reduction characteristics and flow field analysis of textured surface,” *Friction*, vol. 4, no. 2, pp. 165–175, 2016.

[3] D. Reduction, “Applications of Water-Soluble Polymers in Turbulent Drag Reduction,” *Processes*, vol. 5, no. 2, p. 24, 2017.

[4] B. Dean and B. Bhushan, “Shark-skin surfaces for fluid-drag reduction in turbulent flow: A review,” *Philos. Trans. R. Soc. A Math. Phys. Eng. Sci.*, vol. 368, no. 1929, pp. 4775–4806, 2010.

[5] K. B. Golovin, J. W. Gose, M. Perlin, S. L. Ceccio, and A. Tuteja, “Bioinspired surfaces for turbulent drag reduction Subject Areas :,” *Philos. Trans. R. Soc. A*, vol. 374, no. 2073, 2016.

[6] G. D. Bixler and B. Bhushan, “Fluid drag reduction with shark-skin riblet inspired microstructured surfaces,” *Adv. Funct. Mater.*, vol. 23, no. 36, pp. 4507–4528, 2013.

[7] D. C. Chu and G. E. Karniadakis, “A direct numerical simulation of laminar and turbulent flow over riblet-mounted surfaces,” *J. Fluid Mech.*, vol. 250, pp. 1–42, 1993.

[8] R. García-Mayoral and J. Jiménez, “Drag reduction by riblets,” *Philos. Trans. R. Soc. A Math. Phys. Eng. Sci.*, vol. 369, no. 1940, pp. 1412–1427, 2011.

[9] S. Raayai-Ardakani and G. H. McKinley, “Drag reduction using wrinkled surfaces in high Reynolds number laminar boundary layer flows,” *Phys. Fluids*, vol. 29, no. 9, 2017.

[10] C. Lee, C. H. Choi, and C. J. Kim, “Superhydrophobic drag reduction in laminar flows: a critical review,” *Exp. Fluids*, vol. 57, no. 12, pp. 1–20, 2016.

[11] J. Ou, B. Perot, and J. P. Rothstein, “Laminar drag reduction in microchannels using ultrahydrophobic surfaces,” *Phys. Fluids*, vol. 16, no. 12, pp. 4635–4643, 2004.

[12] T. J. Kim and C. Hidrovo, “Pressure and partial wetting effects on superhydrophobic friction reduction in microchannel flow,” *Phys. Fluids*, vol. 24, no. 11, 2012.

[13] T. J. Kim, R. Kanapuram, A. Chhabra, and C. Hidrovo, “Thermo-Wetting and Friction Reduction Characterization of Microtextured Superhydrophobic Surfaces,” *J. Fluids Eng.*, vol. 134, no. 11, p. 114501, 2012.

[14] P. F. Hao, C. Wong, Z. H. Yao, and K. Q. Zhu, “Laminar drag reduction in hydrophobic microchannels,” *Chem. Eng. Technol.*, vol. 32, no. 6, pp. 912–918, 2009.

[15] G. Daschiel, M. Perić, J. Jovanović, and A. Delgado, “The holy grail of microfluidics: Sub-laminar drag by layout of periodically embedded microgrooves,” *Microfluid. Nanofluidics*, vol. 15, no. 5, pp. 675–687, 2013.

[16] A. Gaddam, B. S. Kattemalalawadi, A. Agrawal, and S. S. Joshi, “Demarcating wetting states in textured microchannels under flow conditions by Poiseuille number,” *Microfluid. Nanofluidics*, vol.

21, no. 8, pp. 1–16, 2017.

[17] J. Zhang, Z. Yao, and P. Hao, “Formation and evolution of air–water interfaces between hydrophilic structures in a microchannel,” *Microfluid. Nanofluidics*, vol. 21, no. 8, pp. 1–8, 2017.

[18] B. R. Solomon, K. S. Khalil, and K. K. Varanasi, “Drag reduction using lubricant-impregnated surfaces in viscous laminar flow,” *Langmuir*, vol. 30, no. 36, pp. 10970–10976, 2014.